CHEMIJA
2026. Vol. 37. No. 1. P. 18–28

ISSN 0235-7216 eISSN 2424-4538
DOI: https://doi.org/10.6001/chemija.2026.37.1.3

The effect of gold nanorod dimensions on the electrochemical performance of an enzymatic glucose biosensor

Marina Šapauskienė,

Asta Kaušaitė-Minkštimienė,

Almira Ramanavičienė,

Anton Popov*

NanoTechnas – Center of Nanotechnology and Materials Sciences,
Faculty of Chemistry and Geosciences,
Vilnius University,
24 Naugarduko Street,
03225 Vilnius, Lithuania

The nanostructuring of electrode surfaces is commonly employed to enhance the electrochemical performance of enzymatic glucose biosensors. However, the optimisation of nanostructure morphology and dimensions remains an incompletely explored area. In this work, three colloidal solutions of gold nanorods (AuNR), different in size, were synthesised. SEM analysis revealed that nanorods exhibited distinct lengths: 32.8 ± 3.4 nm for $AuNR_I$, 35.0 ± 3.5 nm for $AuNR_{II}$ and 90.0 ± 6.7 nm for $AuNR_{III}$. Glucose biosensors based on graphite rod electrodes modified with AuNR and glucose oxidase showed enhanced electrochemical performance. Notably, biosensors fabricated with $AuNR_I$ and $AuNR_{III}$ achieved similar maximal current changes during the enzymatic reaction (ΔI_{max} = 49.31 ± 2.64 and 48.45 ± 2.35 μA, respectively), despite the pronounced difference in the electroactive surface area obtained after AuNR deposition (0.082 ± 0.009 and 0.194 ± 0.005 cm^2, respectively). Moreover, the fabricated glucose biosensor based on $AuNR_I$ exhibited a linear range of practical relevance (0.1–8 mM), a low limit of detection (4.6 μM), and is suitable for glucose detection in the diluted blood serum. Overall, the results indicate that morphological characteristics, including size, aspect ratio, and spatial organisation, play a crucial role in optimising the design and performance of enzymatic glucose biosensors.

Keywords: glucose biosensor, enzyme, gold nanorods, electrochemical detection

INTRODUCTION

Diabetes mellitus is one of the most prevalent metabolic disorders worldwide: almost half a billion people are living with it, and the number is expected to increase by 25% in 2030 and 51% in 2045 [1]. Therefore, the effective management of the disease relies heavily on the accurate and continuous monitoring of blood glucose levels. As a result, the development of reliable glucose biosensors remains a key focus in biomedical diagnostics. Glucose oxidase (GOx)-based enzymatic biosensors have long been regarded as the gold standard due to their high specificity toward β-D-glucose and suitability for electrochemical biosensor fabrication. However, improving their analytical performance, particularly sensitivity and stability in physiologically relevant environments, continues to be an essential challenge [2]. The rapid progress in nanomaterials has opened new routes to enhancing electron transfer efficiency and catalytic activity in enzymatic glucose biosensing platforms [3].

Gold nanomaterials, such as gold nanorods (AuNR), have attracted a significant interest due to their unique physicochemical properties, including a high surface-to-volume ratio, suitability

* Corresponding author. Email: anton.popov@chgf.vu.lt

for biomolecule immobilisation, an excellent biocompatibility, and tunable optical and electronic characteristics [4, 5]. A defining feature of AuNR is their localised surface plasmon resonance (LSPR) bands, which can be precisely tuned by modifying the nanorod size and aspect ratio [6]. This optical tunability of the LSPR makes AuNR particularly attractive for a wide range of biomedical and sensing applications, as resonance within the biological transparency window (650–900 nm) enables an enhanced light penetration and a minimal photothermal damage to biological tissues [7]. Such properties also correlate with electronic behaviour, influencing charge-transfer processes and catalytic efficiency when AuNRs are integrated into enzymatic electrochemical biosensors [8–12].

Various strategies of the synthesis have been developed to obtain AuNR with the controlled size and desirable optical properties [13–17]. Despite a significant progress, correlations between the synthesis method, the resulting nanorod size, and the biosensor performance remain insufficiently explored. In particular, understanding how subtle morphological variations influence enzyme immobilisation efficiency, electron transfer between GOx and the electrode surface, and the overall analytical response is essential for the rational design of high-performance glucose sensors.

Enzymatic biosensors based on AuNR have shown promising analytical characteristics, including a high sensitivity, low detection limits, a rapid response, and a strong resistance to interfering species such as ascorbic acid, uric acid, and additional saccharides [8–11]. The intrinsic selectivity of GOx, combined with the catalytic and conductive properties of AuNR, provides a valuable platform for glucose detection in complex biological matrices. Importantly, the capability of AuNR-modified electrodes to maintain performance in human serum or similar environments highlights their potential for translation into practical biomedical devices [8–11].

In this study, AuNR were synthesised using two distinct methods to obtain nanomaterials with different dimensions. Their morphological and LSPR properties were characterised to validate the formation of nanorods and evaluate the material quality. Three types of synthesised AuNR were applied to improve the analytical characteristics of a glucose biosensor based on a graphite rod electrode (GRE) modified with AuNR and GOx. Taken together, this work investigated how variations in AuNR dimensions influence the analytical performance of electrochemical enzymatic glucose biosensors.

EXPERIMENTAL SECTION

Materials

L-ascorbic acid (AA, Fluka, 99.7%), cetyltrimethylammonium bromide (CTAB, Carl Roth, 99%), D-(-)-fructose (Merck, 99%), D-(+)-galactose (Carl Roth, 98%), D-(+)-glucose (Sigma-Aldrich, 99.5%), glucose oxidase (GOx, from *Aspergillus niger* (EC.1.1.3.4.) of 360 U mg^{-1} activity, ROTH), glutaraldehyde (25%, Carl Roth), graphite rods (diameter 3.0 mm, 99.995%, Sigma-Aldrich), hydrochloric acid (HCl, 37% wt%, Carl Roth), hydrogen tetrachloroaurate(III) trihydrate ($HAuCl_4 \times 3H_2O$, Glenthams, 99.9%), hydroquinone (Carl Roth, 99.5%), D-(+)-mannose (Carl Roth, 99%), phenazine methosulfate (PMS, Thermo Scientific Chemicals, 98%), phosphate buffered saline tablets (PBS, Carl Roth), potassium chloride (KCl, Carl Roth, 99%), potassium hexacyanoferrate ($K_3[Fe(CN)_6]$, Sigma-Aldrich, 98.5%), silver nitrate ($AgNO_3$, Carl Roth, 99.9%), sodium borohydride ($NaBH_4$, Carl Roth, 97%), sucrose (Fluka, 99%), uric acid (UA, Sigma Aldrich, 99%) and blood serum (from human male AB plasma, Sigma-Aldrich).

AuNR synthesis

$AuNR_I$ and $AuNR_{II}$ were prepared using a previously reported two-step seed-mediated synthesis method [15]. Seeds were synthesised by adding 800 µL of a cold 10 mM $NaBH_4$ solution to a 2 mL mixture of 0.1 M CTAB and 2.5 mM $HAuCl_4$ solution, which had been prewarmed to 35°C. The seeds solution was left for 1 h at 35°C. The growth solution was prepared by combining 5 mL of 0.2 M CTAB and 5 mL of 1 mM $HAuCl_4$ solutions. Subsequently, 60 or 160 µL of 5 mM $AgNO_3$ solution was added to the mixture to prepare $AuNR_I$ and $AuNR_{II}$ solutions, respectively. $AuNR_I$ and $AuNR_{II}$ syntheses were proceeded in the same way. The stirred mixtures became transparent after the addition of 55 µL of 0.1 M ascorbic acid solution and were then left in the thermostat at 35°C for 5 min. Eventually, 12 µL of the seed solution was slowly added to the stirred growth solution and incubated at 35°C for 24 h. After the incubation, the AuNR

solution was washed by centrifugation at 7000 × g for 20 min. The AuNR solution was washed twice with distilled water and diluted to a final volume of 5 mL with a 0.1 M CTAB solution.

$AuNR_{III}$ synthesis started by pouring 2.4 mL of 0.01 M $HAuCl_4$, 960 µL of 0.02 M $AgNO_3$, 270 µL of 1 M HCl, and 720 µL of 0.33 M hydroquinone solutions into 5 mL of 0.1 M CTAB [13]. The resulting mixture was preheated at 35°C. Then, 3 mL of cold 0.5 mM $NaBH_4$ solution was added. After 24 h, the solution was washed by centrifugation at 10000 × g for 10 min. The AuNR solution was washed 2 times with distilled water and once with 0.1 M CTAB. After the centrifugation, the solution was diluted to 5 mL with 0.1 M CTAB.

AuNR characterisation

The absorbance spectra of AuNR solutions were recorded using a Cary 5000 UV-Vis-NIR spectrophotometer in a range of 400–1400 nm or a Shimadzu UV 1900i spectrophotometer in a range of 400–1000 nm. AuNR morphology was examined using a Hitachi SU-70 high-resolution field emission scanning electron microscope SU-70 (FE-SEM). Before the SEM analysis, AuNR solutions were washed 4 times by centrifugation with distilled water to remove residual surfactants and impurities.

Pre-treatment and modification of electrodes

Graphite rods were mechanically polished sequentially with a fine, very fine and ultra-fine grit sandpaper, rinsed with deionized water, and air-dried at room temperature. To prevent the side-surface contact with electrolyte during electrochemical measurements, graphite rods were enclosed in a silicone tubing. The working electrode geometric surface area was 0.071 cm^2. Three types of modified electrodes – GRE/$AuNR_I$/GOx, GRE/$AuNR_{II}$/GOx and GRE/$AuNR_{III}$/GOx – were prepared. For each modification, 3 µL of $AuNR_I$, $AuNR_{II}$, or $AuNR_{III}$ solution was drop-cast on the bare GRE surface and allowed to dry at room temperature. Subsequently, 3 µL of a 40 mg mL^{-1} GOx solution was deposited onto the AuNR-modified GRE surface. The resulting GRE/AuNR/GOx were exposed to the vapour of a 25% glutaraldehyde solution for 15 min to immobilise GOx via cross-linking, then rinsed with distilled water to remove an unbound enzyme. After air-drying, the modified electrodes were placed over the buffer solution and stored at 4°C until electrochemical measurements were performed.

Electrochemical measurements

Electrochemical measurements were performed using a PalmSens4 potentiostat (PalmSens BV, The Netherlands) with the PSTrace 5.11 software. A three-electrode system comprised of an AuNR-GOx modified GRE as the working electrode, a platinum wire as the counter electrode, and an Ag/AgCl (3 M KCl) as the reference electrode (Metrohm, Switzerland). All aqueous solutions were prepared with ultrapure distilled water. A 0.5 M D-glucose solution was prepared 24 h before the experiments to allow the complete mutarotation.

Chronoamperometric measurements were carried out at a constant potential of +0.3 V vs Ag/AgCl (3 M KCl) in an electrochemical cell containing 5 mL of 50 mM PBS (pH 6.0) with 0.1 M KCl and 6 mM PMS as a redox mediator. During PMS-mediated glucose oxidation, the flavin adenine dinucleotide (FAD) cofactor in GOx is reduced to $FADH_2$ and subsequently reoxidised by PMS. The reduced PMS species then donate electrons to the electrode surface, regenerating the oxidised mediator and producing a measurable anodic current. The cell solution was stirred at 400 rpm throughout the measurements. After the baseline stabilisation, predetermined glucose volumes were added to the cell. The resulting anodic current change (ΔI) was recorded as the biosensor signal, calculated as the difference between the steady-state current after glucose addition and the baseline current.

Cyclic voltammetry (CV) was performed in a 50 mM PBS solution (pH 6.0) containing 2.5 mM $[Fe(CN)_6]^{3-/4-}$, scanning potentials from –0.2 to +0.7 V at sweep rates of 10, 25, 50, 75, 100 and 150 mV s^{-1}. The 3th cycle of cyclic voltammograms was used to evaluate the electrochemically active surface area (EASA). The EASA calculations were based on the Randles–Sevcik equation

$$i = 2.69 \times 10^5 \times n^{\frac{3}{2}} \times A \times D^{\frac{1}{2}} \times C \times v^{\frac{1}{2}},$$

where i_p is the maximum peak current (A), n is the number of electrons transferred during the redox event, A is EASA (cm^2), D is the diffusion coefficient ($cm^2 \cdot s^{-1}$, $6.40 \cdot 10^{-6}$ $cm^2 \cdot s^{-1}$ for ferrocyanide), C is the concentration of electroactive species ($mol \cdot cm^{-3}$), and v is the potential sweep rate ($V \cdot s^{-1}$).

All electrochemical measurements were performed at room temperature, and the results are reported as the mean value of at least three independent experiments. Data analysis was conducted to determine the intercept, slope, and determination coefficient of the calibration curve, as well as to calculate the limit of detection (LOD), the maximal current change during the enzymatic reaction (ΔI_{max}), and the apparent Michaelis constant ($K_{M(app)}$). The parameters ΔI_{max} and $K_{M(app)}$ were obtained as coefficients a and b of the hyperbolic function $y = ax/(b + x)$, which was applied to fit the experimental data. The LOD was calculated based on the equation LOD = 3σ/*S*, where σ is the standard deviation of the sample with the lowest glucose concentration response, and *S* is the slope of the calibration curve.

RESULTS

Three types of AuNR were synthesised using two different synthesis methods to obtain nanostructures with tunable optical and morphological characteristics. The optical properties of the synthesised AuNR were evaluated by UV–Vis absorption spectroscopy (Fig. 1). All samples exhibited two characteristic LSPR bands: one appearing near 520 nm and another, the position of which varied depending on the aspect ratio of the nanorods. Specifically, the LSPR peaks were observed at 520 and 670 nm for $AuNR_I$, at 525 and 740 nm for $AuNR_{II}$, and at 517 and 1258 nm for $AuNR_{III}$. This optical tunability of the LSPR makes AuNR particularly attractive for a wide range of biomedical and sensing applications, as resonance within the biological transparency window (650–900 nm) enables enhanced light penetration and minimal photothermal damage to biological tissues [7]. The presence of two distinct LSPR bands confirms the anisotropic nature of the synthesised nanostructures. For spherical nanoparticles, a single LSPR band is typically observed; however, nanorods, as anisotropic nanoparticles, display two distinct resonances corresponding to the oscillation of conduction electrons along the short and long axes of the structure [18, 19]. Also, the second LSPR peak is more pronounced than the first peak, indicating that the colloidal solution is predominantly composed of nanorods [20].

The strong red shift observed for $AuNR_{III}$ indicates a significantly higher aspect ratio (6.98) compared to those of $AuNR_I$ (2.73) and $AuNR_{II}$ (3.22), which is consistent with the morphological data obtained from SEM analysis (Fig. 2). The distinct differences in LSPR peak positions and intensities among the three AuNR types directly reflect variations in their shape anisotropy and provide a valuable insight into the relationship between nanorods geometry and plasmonic behaviour.

The SEM analysis confirmed a well-defined rod-shaped geometry. The dimensional analysis of AuNR

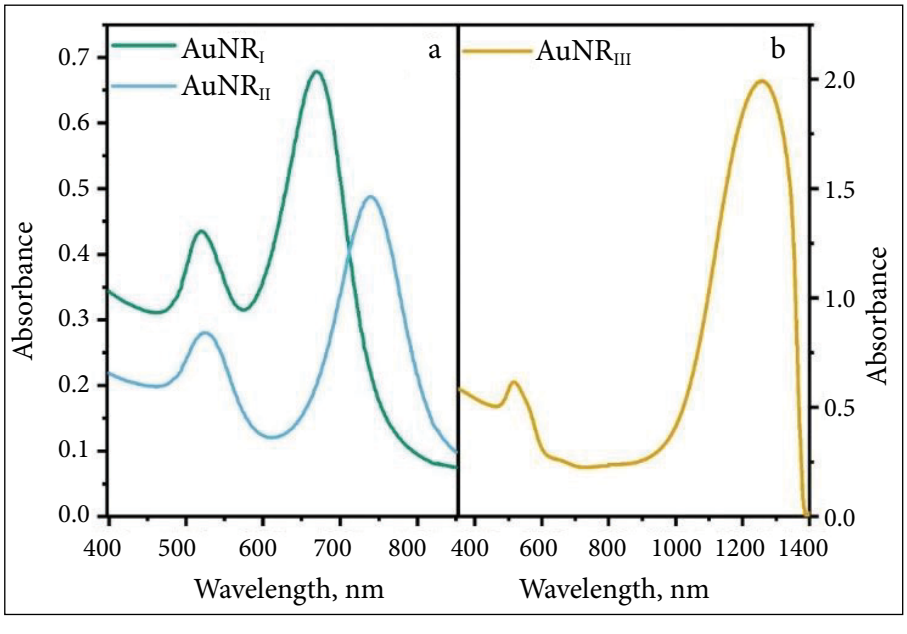

Fig. 1. UV–Vis absorbance spectra of (a) $AuNR_I$ and $AuNR_{II}$, and (b) $AuNR_{III}$

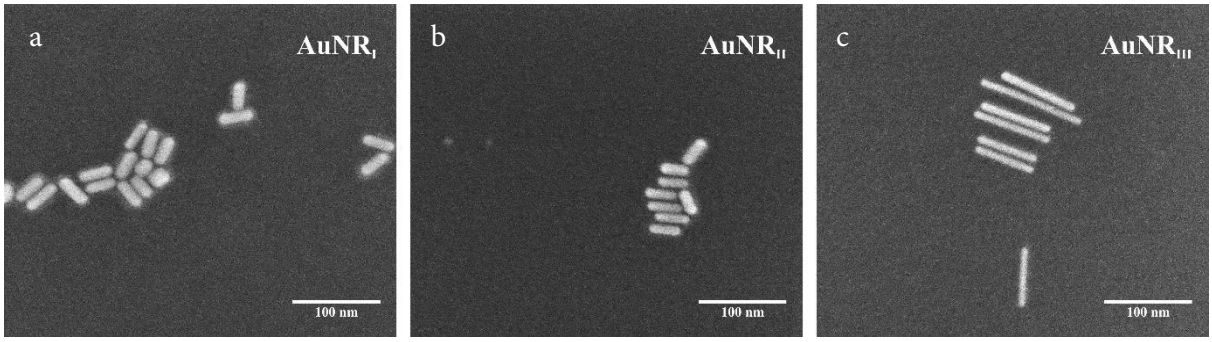

Fig. 2. SEM images of (a) AuNR$_I$, (b) AuNR$_{II}$ and (c) AuNR$_{III}$

was performed using the ImageJ software to calculate their length and width from the representative SEM micrographs (Table 1). As both AuNR$_I$ and AuNR$_{II}$ were yielded via a seed-mediated synthesis method, their comparable dimensions resulted in similar aspect ratios of 2.73 and 3.21, respectively. In contrast, AuNR$_{III}$, obtained through seedless (one-pot) synthesis using hydroquinone as a reducing agent, exhibited a significantly greater aspect ratio – 6.98. Although all three synthesised AuNR have very similar widths, their lengths differed considerably, as AuNR$_{III}$ were 2.74 and 2.57 times longer than AuNR$_I$ and AuNR$_{II}$, respectively.

The seed-mediated growth method of AuNR typically ensures the controlled nucleation and gradual elongation of nanorods, resulting in moderate aspect ratios and a high monodispersity [15–17]. This two-step synthesis method involves the preparation of gold seeds through the rapid reduction of Au^{3+} ions using sodium borohydride, followed by their subsequent enlargement in a growth solution containing Au(III)-CTAB, which is reduced to Au^{+} ions by ascorbic acid in the presence of silver nitrate [15]. The ascorbic acid concentration used in the growth solution is a critical parameter that significantly impacts the growth of nanorods. Typically, the ascorbic acid concentration should be maintained at approximately 1.1 times the molar concentration of Au^{3+} ions to ensure a directional growth and prevent an uncontrolled secondary nucleation, which is crucial for producing high-quality AuNR [21]. Although widely adopted, the classical seed-mediated synthesis has a significant limitation: the position of the second LSPR peak generally does not exceed 850 nm, restricting applicability in systems that require a deeper NIR responsiveness [15]. To overcome this constraint, a novel reducing agent, hydroquinone, was proposed to replace ascorbic acid in the seed-mediated growth of AuNR, thereby increasing the synthesis yield and shifting the LSPR peak position from 770 up to 1230 nm [14]. Using a 10–20-fold excess of gold concentration compared to the gold concentration slows the anisotropic growth process, allowing for the precise tuning of nanorods dimensions. This behaviour is well aligned with a principle that the kinetic rate of gold reduction, modulated by the strength of the reducing agent, is tightly linked to the degree of anisotropic crystal growth [22]. For example, the hydroquinone-based seedless approach facilitates a slower reduction rate and anisotropic growth along the longitudinal axis, yielding more elongated nanorods with extended LSPR bands in the NIR region [13]. Additionally, silver ions influence both the aspect ratios and the position of the LSPR peak of AuNR by selectively binding to specific assets of growing nanorods [20]. In the present study, the final $AgNO_3$ concentration in the synthesis of AuNR$_{III}$ was more than 500 times higher compared to that in the syntheses of AuNR$_I$ and AuNR$_{II}$.

To evaluate how the modification of GRE with synthesised AuNR influences the EASA of the electrode, CV measurements were performed using

Table 1. **Size distribution and aspect ratios of the synthesised AuNR**

AuNR type	Length, nm	Width, nm	Aspect ratio
AuNR$_I$	32.8 ± 3.4	12.0 ± 2.2	2.73
AuNR$_{II}$	35.0 ± 3.5	10.9 ± 2.0	3.21
AuNR$_{III}$	90.0 ± 6.7	12.9 ± 3.0	6.98

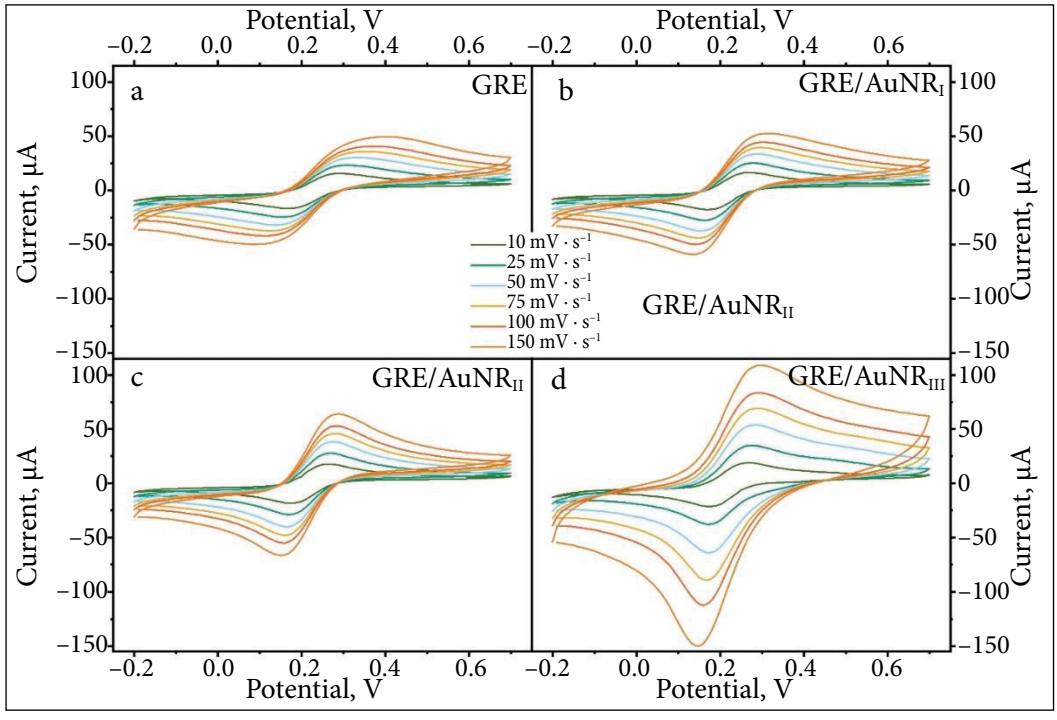

Fig. 3. The third cycle of cyclic voltammograms of GRE (a), GRE/AuNS$_I$ (b), GRE/AuNR$_{II}$ (c) and GRE/AuNS$_{III}$ (d) recorded at different electrode potential sweep rates in a PBS solution containing 2.5 mM $[Fe(CN)_6]^{3-/4-}$

the ferri/ferrocyanide redox probe. The resulting voltammograms are presented in Fig. 3. An apparent increase in the peak current was observed upon modification of the GCE with AuNR, confirming a substantial enhancement in charge transfer capacity relative to the bare electrode. The current response continuously increased with nanorod length, with AuNR$_{III}$ producing the most significant enhancement, which reflects the high number of electroactive sites provided by these structures.

Cyclic voltammograms obtained at different scan rates (10–150 mV s^{-1}) demonstrate a well-defined oxidation and reduction peaks of a similar magnitude. The peak-to-peak separation increased with the scan rate, characteristic of a diffusion-controlled quasi-reversible process. The anodic peak current showed a linear relationship with the square root of the potential sweep rate (Fig. 4), supporting this kinetic interpretation.

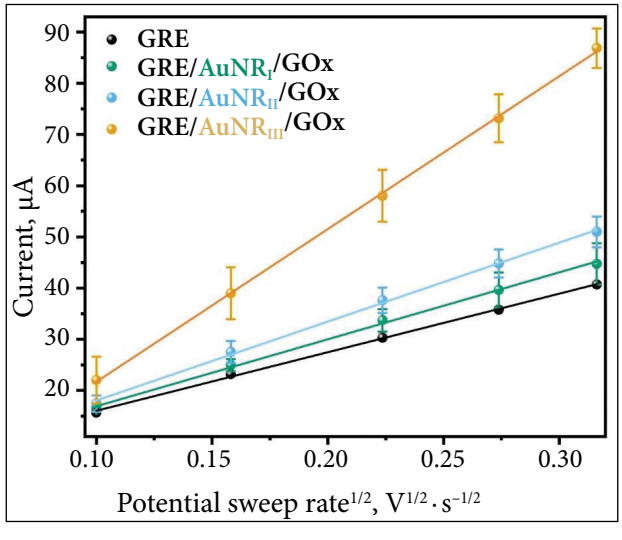

Fig. 4. The relationship between the square root of the potential sweep rate and the peak anodic current

The EASA of each AuNR-modified GRE was calculated from the obtained voltammograms according to the Randles–Sevcik equation, as described in the Electrochemical Measurements section. The slope of the linear fit between the anodic peak current and the square root of the potential scan rate reflected the differences in EASA among the tested electrodes.

The obtained EASA values increased progressively from $AuNR_I$ to $AuNR_{III}$, following the trend: 0.082 ± 0.009, 0.098 ± 0.004 and 0.194 ± 0.005 cm^2 (Table 2). This increase clearly indicates that electrode modification with AuNR enhances the electroactive surface area compared to the bare graphite electrode (EASA = 0.070 ± 0.003 cm^2, geometric area = 0.071 cm^2). The deposition of AuNR, therefore, provides a measurable enlargement of the electrochemically active interface, enabling more efficient charge transfer processes. This tendency correlates with the morphology of the synthesised nanorods, as the longest $AuNR_{III}$ (90.0 ± 6.7 nm) provided the largest EASA. In contrast, the shorter $AuNR_I$ (32.8 ± 3.4 nm) and $AuNR_{II}$ (35.0 ± 3.5 nm) resulted in lower values. The widths of the nanorods were relatively similar – 11.98 ± 2.16, 10.86 ± 2.03, and 12.87 ± 3.04 nm.

Table 2. **Calculated EASA of various electrodes. Error bars are expressed as sample standard deviation ($n = 3$)**

Electrode type	EASA, cm^2
GRE	0.070 ± 0.003
GRE/$AuNR_I$	0.082 ± 0.009
GRE/$AuNR_{II}$	0.098 ± 0.004
GRE/$AuNR_{III}$	0.194 ± 0.005

The following observations are consistent with the data reported in the literature, where AuNR of a comparable length demonstrated greater electrochemical activity when their aspect ratio increased [23]. AuNR with similar lengths, but varying widths, were examined. It was shown that rods with larger aspect ratios generated a stronger electrochemical responses, whereas narrower AuNR produced smaller increases in the EASA. These insights emphasise that not only the presence of AuNR, but also their morphological properties strongly influence charge transport efficiency at the electrode–electrolyte interface.

It should be noted that the AuNR dispersions were not unified in terms of AuNR concentration, gold amount, or optical density, meaning that the actual mass of gold deposited on the electrode differed among $AuNR_I$, $AuNR_{II}$ and $AuNR_{III}$. Therefore, while the observed increase in EASA follows the trend of increasing aspect ratio, it can also partially reflect variations in nanorods loading during electrode modification. Moreover, the results demonstrate a clear enhancement of electrochemical surface properties following AuNR deposition.

Given that electrode nanostructuring strongly determines charge transfer efficiency, the next stage of this study focused on assessing how the morphology of AuNR affects the electrochemical performance of enzymatic glucose biosensor. The working electrode modification steps and electrochemical measurements are presented in the Scheme.

This analysis aimed to determine whether increased EASA alone drives improved biosensor response, or whether an optimal balance between the surface area, charge-transfer efficiency, and enzyme–nanostructure interaction is necessary to ensure the best analytical performance. Chronoamperometric measurements were held to evaluate the electrochemical performance of three types of modified electrodes – GRE/$AuNR_I$/GOx, GRE/$AuNR_{II}$/GOx and GRE/$AuNR_{III}$/GOx – as a proposed model for glucose biosensor development (Fig. 5).

Among all electrodes evaluated, the $AuNR_I$-modified GRE exhibited the highest current response (ΔI_{max} = 49.31 ± 2.64 μA) and produced the least measurement variability, as evidenced by the lowest associated error bars. The $AuNR_{II}$-based biosensor showed an ΔI_{max} of 37.86 ± 1.23 μA, while the $AuNR_{III}$-based one yielded 48.45 ± 2.35 μA. $K_{M(app)}$ was determined to be 10.8 ± 0.8, 6.7 ± 0.7 and 10.2 ± 0.9 mM for working electrodes prepared using $AuNR_I$, $AuNR_{II}$ and $AuNR_{III}$, respectively. Moreover, all three types of biosensors tested exhibited a linear range from 0.1 to 8 mM, with a determination coefficient (R^2) of 0.996. Despite the most significant EASA and the highest aspect ratio of $AuNR_{III}$, GRE/$AuNR_{III}$/GOx exhibited a slightly lower amperometric response compared to GRE/$AuNR_I$/GOx. The higher electrochemical activity of $AuNR_I$ can be attributed to their optimised aspect

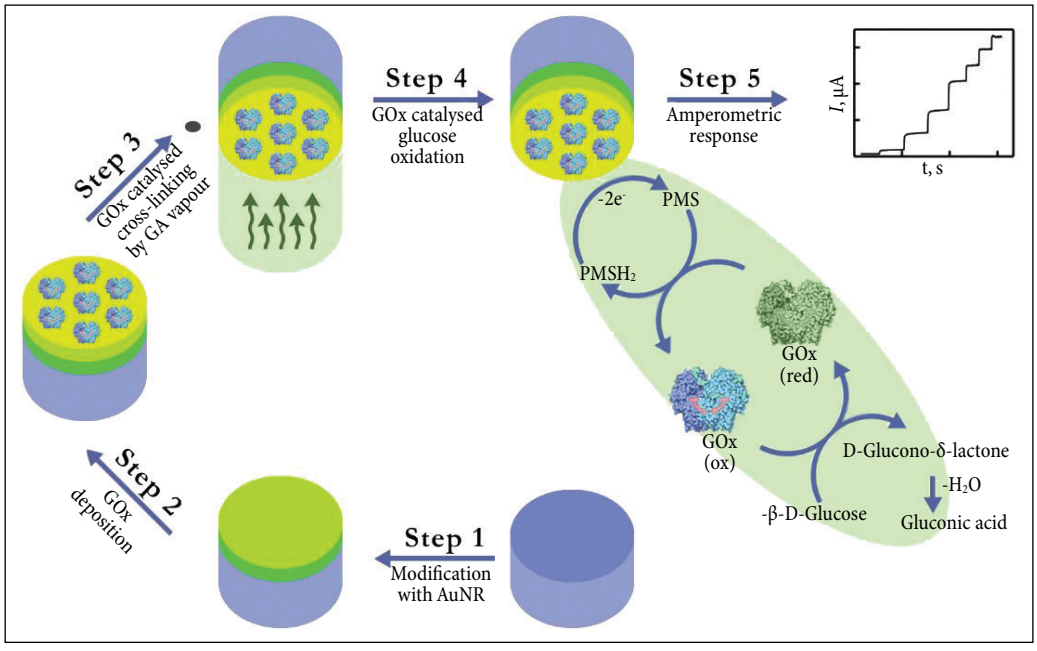

Scheme. Schematic overview of the working electrode preparation and electrochemical determination of glucose concentration

ratio and desirable surface morphology, which enable better GOx immobilisation, faster electron transfer and more effective interaction between the enzyme layer and the nanostructured surface. The correlation between morphology and EASA highlights the significant impact of nanoscale geometry on electrode functionality. An increase in EASA does not necessarily mean higher analytical signals, as an excessive elongation or an uneven surface coverage may induce aggregation, hinder a uniform electron transport, or restrict enzyme accessibility on the electrode surface. These results highlight that an optimal nanorod morphology, providing both adequate surface area and efficient charge-transfer properties, is essential for achieving higher biosensor analytical signal. In

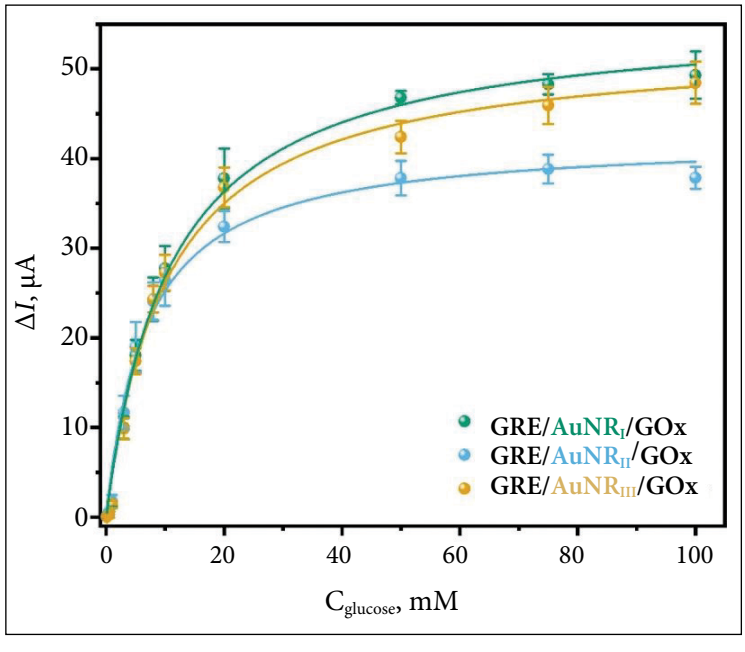

Fig. 5. Dependence of the current response on the glucose concentration of the biosensors based on the GRE/AuNR/GOx, modified with different types of AuNR

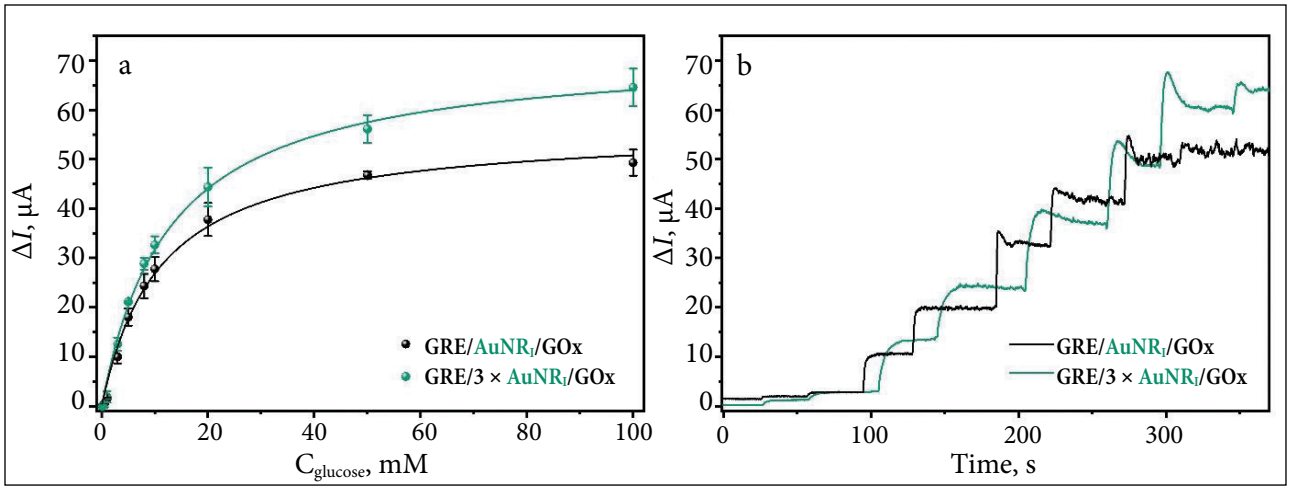

Fig. 6. Calibration plots (a) and the dependence of current response on the glucose concentration (b) for the biosensors based on GR/AuNR$_l$/GOx using various concentrations of AuNR$_l$

this context, the surface concentration of AuNR could also play a critical role in determining biosensor performance. To assess this effect, a working electrode modified with a three-fold higher AuNR$_l$ concentration (GRE/3×(AuNR$_l$)/GOx) was fabricated. The corresponding electrochemical measurements are shown in Fig. 6a.

Notably, tripling the AuNR$_l$ concentration increased ΔI_{max} by 1.31 times, reaching 64.54 ± 3.79 μA. Moreover, modification with AuNR$_l$ provided a fast and reliable chronoamperometric response (Fig. 6b). These results confirmed that, in addition to selecting an appropriate AuNR size, optimising the surface concentration of the nanostructures is essential. This observation is consistent with previous reports indicating that an increased electroactive surface area does not always result in improved analytical performance of biosensors [8, 24]. In addition, the electron transfer rate, enzyme–nanostructure interactions, the morphology of the nanostructures, and the spatial distribution of nanomaterials on the electrode are factors of high importance to the registered analytical signal [9–11, 24, 25]. Previous studies have shown that elongated or densely packed gold nanostructures may exhibit large EASA values but produce lower current responses due to restricted enzyme accessibility or hindered charge transport. These tendencies align with the present results, confirming that optimising the AuNR size provides the most effective balance of surface area and charge-transfer properties, ultimately enhancing overall biosensor performance.

Following the evaluation of amperometric performance, the selectivity of the developed glucose biosensor was tested, as selectivity is one of the key parameters determining the analytical applicability of enzymatic biosensors. To assess potential interference, structurally related carbohydrates were sequentially introduced to the electrochemical cell at a concentration of 5 mM. The compounds were added in the following order: glucose (the first addition), fructose, mannose, galactose, sucrose and glucose (the second addition). After each addition, the current response was recorded once a steady-state signal was reached (Fig. 7).

As can be seen, only glucose induced an amperometric response, whereas the presence of other saccharides resulted in negligible changes in current. These results clearly demonstrate that the developed glucose biosensor exhibits outstanding selectivity towards glucose, attributed to the enzymatic recognition of glucose and the favourable electron-transfer environment provided by the AuNR-modified surface.

Considering the potential real-world applications of the developed glucose biosensor, it is essential to examine the biochemical context in which glucose monitoring typically occurs. Chronoamperometric measurements (Fig. 7) demonstrated that the glucose biosensor maintained an excellent selectivity, with amperometric responses unaffected by tested carbohydrates except for glucose. However, physiological fluids contain various electroactive compounds, which can potentially interfere with glucose detection.

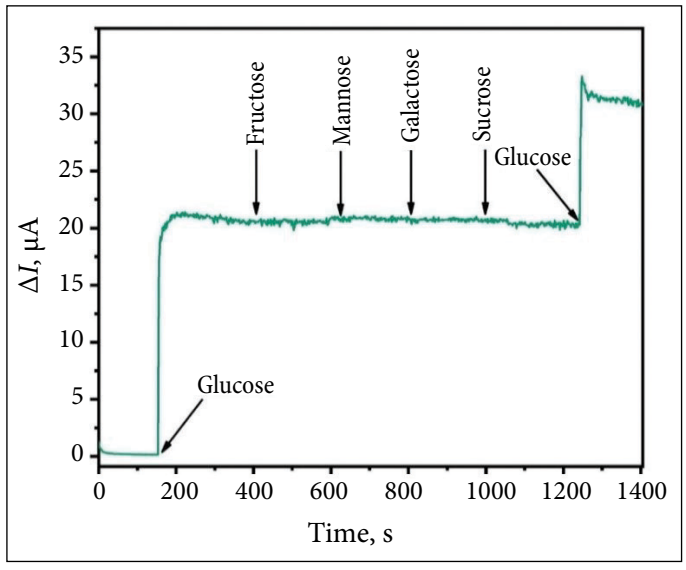

Fig. 7. Current response of the biosensor based on a GE/AuNR$_l$/GOx electrode to 5 mM of glucose, followed by the addition of 5 mM of fructose, 5 mM of mannose, 5 mM of galactose, 5 mM of sucrose, and again 5 mM of glucose

Hyperuricemia and type 2 diabetes mellitus are closely related: each of these diseases increases the risk of the other. Several antidiabetic drugs, including insulin, sitagliptin and alogliptin, have been reported to elevate serum uric acid (UA) levels [26–29]. Therefore, to further assess the suitability of the developed glucose biosensor, glucose detection experiments were performed in the diluted commercial human blood serum in the presence of common electroactive interferents, such as uric acid and ascorbic acid (AA), which are typically present in physiological fluids. In 10 times diluted serum spiked with 5 mM glucose, the measured glucose concentration was 5.18 ± 0.06 mM with a 103.6% recovery ratio. The addition of 0.2 mM of AA and 0.6 mM of UA resulted in a 2.59% increase and a 4.55% decrease in the recorded current, respectively. Considering the 10 times dilution of serum before analysis, the tested UA and AA concentrations are substantially higher than their physiologically achievable levels (UA ≈ 0.042 mM and AA ≈ 0.014 mM in diluted serum [30]). This indicates that any interference from these compounds under real physiological conditions would be significantly lower than that observed in the present experiments. The ability of the biosensor to selectively and reliably detect glucose within such a complex matrix highlights its robustness and practical suitability for real-sample analysis. Moreover, the GRE/AuNR$_l$/GOx-based biosensor exhibited LOD of 4.6 μM, further supporting its applicability for determination in real samples.

CONCLUSIONS

This work examined how the dimensions of AuNS influenced the analytical performance of electrochemical enzymatic glucose biosensors. The results demonstrated that improvements in biosensor response did not correlate directly with the increases in the EASA of the electrode. Notably, biosensors modified with the shortest AuNS$_l$ possessed the highest ΔI_{max}, even though their corresponding EASA was approximately 2.3 times lower than that of electrodes modified with the highest aspect ratio AuNR. Additionally, the electrochemical performance of the biosensor was strongly dependent on the amount of AuNR deposited on the electrode surface.

These findings indicate that optimising enzymatic biosensors based on AuNR requires more than simply maximising EASA. When designing nanostructured sensing interfaces, the morphological characteristics of the nanomaterials, such as the size, aspect ratio, and spatial organisation, are equally critical to achieving an optimal enzyme immobilisation, a high electron-transfer efficiency, and a superior analytical performance.

ACKNOWLEDGEMENTS

This research received funding from the Research Council of Lithuania (LMTLT), Agreement No. S-MIP-24-7.

Received 4 December 2025
Accepted 6 December 2025

References

1. P. Saeedi, I. Petersohn, P. Salpea, et al., *Diabetes Res. Clin. Pract.*, **157**, 107843 (2019).
2. N. Mohamad Nor, N. S. Ridhuan, K. Abdul Razak, *Biosensors*, **12(12),** 1136 (2022).
3. S. J. Kwon, *Nanomaterials*, **13(8)**, 1333 (2023).
4. E. C. Dreaden, A. M. Alkilany, X. Huang, C. J. Murphy, M. A. El-Sayed, *Chem. Soc. Rev.*, **41**, 2740 (2012).
5. K. L. Kelly, E. Coronado, L. L. Zhao, G. C. Schatz, *J. Phys. Chem. B*, **107(3)**, 668 (2003).
6. J. Cao, T. Sun, K. T. V. Grattan, *Sens. Actuators B Chem.*, **195**, 332 (2014).
7. M. Hu, J. Chen, Z. Y. Li, et al., *Chem. Soc. Rev.*, **35**, 1084 (2006).
8. N. German, A. Ramanaviciene, A. Ramanavicius, *Polymers*, **13(13)**, 2173 (2021).
9. N. German, A. Popov, A. Ramanavicius, A. Ramanaviciene, *Biosensors*, **12(8)**, 641 (2022).
10. L. Sakalauskiene, A. Popov, A. Kausaite-Minkstimiene, A. Ramanavicius, A. Ramanaviciene, *Biosensors*, **12(5)**, 320 (2022).
11. L. Sakalauskiene, B. Brasiunas, A. Popov, A. Kausaite-Minkstimiene, A. Ramanaviciene, *Biosensors*, **13(10)**, 942 (2023).
12. F. Zhou, W. Jing, S. Liu, et al., *Mater. Sci. Semicond. Process.*, **105**, 104708 (2020).
13. L. Zhu, Z. Lu, L. Zhang, N. He, *Chin. Chem. Lett.*, **33**, 2491 (2022).
14. L. Vigderman, E. R. Zubarev, *Chem. Mat.*, **25(8)**, 1450 (2013).
15. B. Nikoobakht, M. A. El-Sayed, *Chem. Mat.*, **15(10)**, 1957 (2003).
16. S. O. Obare, N. R. Jana, C. J. Murphy, *Nano Lett.*, **1(11)**, 601 (2001).
17. T. K. Sau, C. J. Murphy, *Langmuir*, **20(15)**, 6414 (2004).
18. X. Huang, S. Neretina, M. A. El-Sayed, *Adv. Mater.*, **21(48)**, 4880 (2009).
19. V. Sharma, K. Park, M. Srinivasarao, *Mater. Sci. Eng. R Rep.*, **65(1–3)**, 1 (2009).
20. P. Chapagain, G. Guisbiers, M. Kusper, et al., *ACS Omega*, **6(10)**, 6871 (2021).
21. C. J. Orendorff, C. J. Murphy, *J. Phys. Chem. B*, **110(9)**, 3990 (2006).
22. N. R. Jana, L. Gearheart, C. J. Murphy, *Adv. Mater.*, **13(18)**, 1389 (2001).
23. C. Zhou, D. Liu, L. Xu, et al., *Sci. Rep.*, **5**, 9939 (2015).
24. B. Brasiunas, A. Popov, G. Kraujelyte, A. Ramanaviciene, *Bioelectrochemistry*, **156**, 108638 (2024).
25. N. German, A. Popov, A. Ramanaviciene, *Biosensors*, **14(3)**, 134 (2024).
26. N. Leung, K. Yip, M. H. Pillinger, M. Toprover, *Mayo Clin. Proc.*, **97(7)**, 1345 (2022).
27. K. W. Lee, D. Shin, *Sci. Rep.*, **12**, 11000 (2022).
28. A. Fuchigami, F. Shigiyama, T. Kitazawa, et al., *Cardiovasc. Diabetol.*, **19**, 1 (2020).
29. Y. Matsushima, Y. Takeshita, Y. Kita, et al., *BMJ Open Diab. Res. Care*, **4**, e000190 (2016).
30. A. Popov, V. Lisyte, M. Sapauskiene, et al., *Mater. Today Nano*, **32**, 100712 (2025).

Marina Šapauskienė, Asta Kaušaitė-Minkštimienė, Almira Ramanavičienė, Anton Popov

AUKSO NANOSTRYPELIŲ MATMENŲ ĮTAKA FERMENTINIO GLIUKOZĖS BIOLOGINIO JUTIKLIO ELEKTROCHEMINIAM VEIKIMUI

S a n t r a u k a

Elektrodų paviršiaus nanostruktūrizavimas dažnai taikomas siekiant pagerinti elektrocheminių fermentinių gliukozės biologinių jutiklių veikimą. Tačiau nanostruktūrų morfologijos ir matmenų optimizavimas vis dar išlieka nepakankamai ištirta sritis. Šiame darbe buvo susintetintos trys skirtingų dydžių aukso nanostrypelių (AuNR) koloidinės suspensijos. SEM analizė parodė, kad nanostrypeliai pasižymėjo panašiu pločiu, tačiau skyrėsi ilgiu: 32,8 ± 3,4 nm ($AuNR_I$), 35,0 ± 3,5 nm ($AuNR_{II}$) ir 90,0 ± 6,7 nm ($AuNR_{III}$). Gliukozės biologiniai jutikliai, paruošti naudojant grafito strypelių elektrodus, modifikuotus AuNR ir gliukozės oksidaze, pasižymėjo geresniu elektrocheminiu veikimu. Svarbu pabrėžti, kad biologiniai jutikliai, paruošti naudojant $AuNR_I$ ir $AuNR_{III}$, parodė panašius didžiausius srovės stiprio pokyčius fermentinės reakcijos metu (ΔI_{max} = 49,31 ± 2,64 ir 48,45 ± 2,35 μA), nors jų elektrochemiškai aktyvaus paviršiaus plotai reikšmingai skyrėsi (atitinkamai 0,082 ± 0,009 ir 0,194 ± 0,005 cm^2). Be to, taikant $AuNR_I$, paruošti gliukozės biologiniai jutikliai pasižymėjo praktiniam naudojimui tinkamu tiesiniu intervalu (0,1–5 mM), maža aptikimo riba (4,6 μM) ir buvo sėkmingai pritaikyti gliukozės nustatymui praskiestame žmogaus serume. Apibendrinant gautus rezultatus galima teigti, kad morfologinės AuNR savybės, tokios kaip dydis, ilgio / pločio santykis ir erdvinis išsidėstymas paviršiuje, yra itin svarbios optimizuojant fermentinių gliukozės biologinių jutiklių struktūrą ir veikimą.